

# Block Matching Frame based Material Reconstruction for Spectral CT

Weiwen Wu, Qian Wang, Fenglin Liu, Yining Zhu, *Member, IEEE*, and Hengyong Yu, *Senior Member, IEEE*

**Abstract**—Spectral computed tomography (CT) has great potential in material identification and decomposition. To achieve high-quality material composition images and further suppress the x-ray beam hardening artifacts, we first propose a one-step material reconstruction model based on Taylor’s first-order expansion. Then, we develop a basic material reconstruction method named material simultaneous algebraic reconstruction technique (MSART). Considering the local similarity of each material image, we incorporate a powerful block matching frame (BMF) into the material reconstruction (MR) model and generate a BMF based MR (BMFMR) method. Because the BMFMR model contains the L0-norm problem, we adopt a split-Bregman method for optimization. The numerical simulation and physical phantom experiment results validate the correctness of the material reconstruction algorithms and demonstrate that the BMF regularization outperforms the total variation and no-local mean regularizations.

**Index Terms**—spectral computed tomography (CT), material reconstruction, block matching frame

## I. INTRODUCTION

THE spectral computed tomography (CT) has attracted continuous attention for its outstanding performance in terms of tissue characterization, lesion detection and material decomposition [1]. The dual energy CT (DECT), as a simple version of spectral CT, has already been widely applied in many applications, such as material decomposition [2], abdomen angiography detection [3, 4], *etc.* The recent development of photon-counting detectors (PCDs) further enhances the prospect of spectral CT. This new-type of PCDs can distinguish the energy of each independently incoming x-ray photon by detecting the electronic pulse signal generated by the peak amplitude of quanta. Because each x-ray photon

energy can be distinguished by thresholding the amplitude of quanta, the transmitted perturbative photon flux can be synchronously recorded within some small energy windows [5]. Theoretically, the measured data of different small energy-windows can be utilized to reconstruct different attenuation maps for the same object [6-8]. Until now, the spectral CT scanners, which are equipped with PCDs whose energy windows are three or greater, have achieved great successes in contrast agent imaging and K-edge imaging [9].

It is very common to use the energy information in the x-ray CT field [10]. For example, the DECT acquires two attenuation intensities using either two different x-ray spectra or two energy windows, and it reconstructs transmission intensity or material images using the collected datasets. Although only limited material component maps can be obtained from the DECT measurements [2], the technique is still of great significance because many materials to be reconstructed only contain two physical processes, i.e., photoelectric effect and Compton scattering. As for the material decomposition of DECT, it usually adopts two or three basis materials [2]. Because the spectral CT utilizes multi-channel projection datasets, it can distinguish more basis materials [11]. The decomposition methods can be mainly divided into two categories: indirect and direct methods.

The indirect material decomposition methods can further be divided into image-based and projection-based methods [12]. For the image-based methods, an intermediate step is performed to reconstruct the channel images from projections [11, 13]. Then, the material decomposition operates on the energy-channel images to obtain the final material maps. For the projection-based methods, the multi-energy projections are first decomposed to the sinograms for basis materials. Then, a conventional FBP or BPF method [14, 15] is employed to reconstruct the material maps. As for the intermediate step of image-based methods, lots of iterative optimization techniques have been proposed [16], such as channel-by-channel reconstruction [17] and joint spatial-spectral correlation reconstruction, tight frame sparsity [18], patch-based low-rank model [1], HighLY constrained backPRojection (HYPR) algorithm [19], spectral prior image constraint compressed sensing (spectral PICCS) technique [20], prior rank and sparsity model [21], tensor dictionary learning (TDL) model [11] and its improved version (L0TDL) [13], nonlocal low-rank and sparse matrix decomposition [22], spatial-spectral cube matching frame (SSCMF) [23], and non-local low-rank cube-based tensor factorization (NLCTF) [24]. Although the intensities of different energy channel images are different, they share the same structure of the scanned object. Thus, global low-rank, sparsity and tensor dictionary are efficient to characterize the structure similarity, leading to better reconstruction results. However, for the image domain

---

This work was supported in part by the National Natural Science Foundation of China (No. 61471070 and No. 61501310), National Instrumentation Program of China (No. 2013YQ030629), NIH/NIBIB U01 grant (EB017140) and China Scholarship Council (No. 201706050070).

W. Wu and F. Liu are with Key Lab of Optoelectronic Technology and Systems, Ministry of Education, Chongqing University, Chongqing 400044, China. Q. Wang and H. Yu are with the Department of Electrical and Computer Engineering, University of Massachusetts Lowell, Lowell, MA 01854, USA. Y. Zhu is with School of Mathematical Sciences, Capital Normal University, Beijing, 100048, China. He is also with Beijing Higher Institution Engineering Research Center of Testing and Imaging, Beijing, 100048, China.

The attributions of W. Wu and Q. Wang are equal. H. Yu serves as the correspondence author (e-mail: [hengyong-yu@ieee.org](mailto:hengyong-yu@ieee.org)).

material decomposition, there are two major unavoidable limitations: (1) because the weighted energy-averaged projections are used to reconstruct channel images, it fails to elaborate the real nonlinear relationship between the polychromatic projections and basic materials, resulting in reduced accuracy of the material decomposition [25]; (2) since the number of energy channels are often smaller than the material types for spectral CT, which means the reconstructed spectral channel images would be decomposed into a greater number of material categories, it may have no unique solutions for material decomposition [26]. For the projection domain material decomposition, the errors in the decomposed basis material sinograms will be magnified in the final material maps, causing serious artifacts.

A direct material decomposition method, i.e., the one-step material reconstruction method [5, 26-28], can directly reconstruct material maps from the multi-energy datasets. For such one-step material reconstruction methods, the energy-dependent material intensity and the proportion of basis material or their product can be linearly modeled [27]. There are two advantages. First, it can exactly describe the spectral imaging process to suppress x-ray beam hardening artifacts in the reconstructed images. Second, the optimization regularization penalty can be directly incorporated into the basis map reconstructions. However, the complexity of the energy spectral transmission model makes the decomposition process unstable, and the results are noticeably sensitive to noise. To improve the signal-to-noise rate (SNR) of reconstructed material maps, the regularizations were incorporated into the one-step material decomposition model, such as total variation (TV) [5], nonlocal TV [26], *etc.*

Because the image structure has self-similarity within a nonlocal region, a Block Matching 3D (BM3D) image model was proposed to characterize such self-similarity by grouping small similar image patches in a given search window [29]. The BM3D algorithm was first introduced for image denoising [30]. Due to its outstanding performance, it was later extended for image deblurring and inpainting [31], *etc.* Regarding image reconstruction, the BM3D was mainly considered as a post-processing procedure [32]. Recently, the BM3D frame was introduced to the MRI image reconstruction field as a powerful regularizer [33].

In this paper, we focus on direct material reconstruction and propose a new one-step material simultaneous algebraic reconstruction technique (MSART) based on the first-order Taylor's expansion for spectral CT. Noting that the same material maps within nonlocal windows may share similar structures, we can improve the accuracy of material reconstruction by considering the structural similarities of material maps. Thus, to incorporate the similarity of material component maps and improve the robustness of the proposed material reconstruction model, the 3D block matching frame [31] is employed as a regularizer for material reconstruction, leading to a Block Matching Frame Material Reconstruction (BMFMR) method. The contributions of this study are three-fold. First, to implement material reconstruction with the one-step procedure, we propose a direct material reconstruction model and develop the MSART based on Taylor's expansion. Second, to obtain better reconstruction results and improve the anti-noising ability of MSART, we incorporate the BMF

regularizer into the MSART model and generate the BMFMR algorithm. Third, to deal with the L0-norm optimization problem in the BMFMR model, we adopt the split-Bregman method. The advantages of BMFMR method are mainly demonstrated in the following three aspects: i) directly obtaining the proportion of each basis material with a one step procedure; ii) having a strong robustness and reducing image artifacts; iii) outperforming TV and non-local mean based material reconstruction methods in terms of image edge information preservation.

The rest of this paper is organized as follows. In section II, we present the model and solution of MSART for spectral CT. In section III, we briefly review the BM3D frame, establish the BMFMR model and adopt the split-Bregman to optimize our objective function. The algorithms and implementation details for comparison are also presented. In section IV, numerical simulations and physical phantom experiments are performed to evaluate the proposed algorithms. In section V, we discuss some related issues and make a conclusion.

## II. MATERIAL MAP RECONSTRUCTION FOR SPECTRAL CT

Let us consider a basic spectral imaging model. The photon number of an x-ray path  $\ell$  from the  $m^{\text{th}}$  energy window  $E_m$  measured by a detector cell can be expressed as

$$w_{m\ell} = \int_{E_m} I_{m\ell}(E) e^{-\int_{r\in\ell} \sum_{n=1}^N \mu_n(E, \mathbf{r}) d\mathbf{r}} dE. \quad (1)$$

Here  $\int_{E_m} dE$  integrates over the range of  $m^{\text{th}}$  energy channel and  $\int_{r\in\ell} d\mathbf{r}$  indicates integral over the x-ray path  $\ell$ . In this work, we assume the imaging object only contains  $N$  materials,  $\mu_n(E, \mathbf{r})$  denotes the  $n^{\text{th}}$  material linear attenuation coefficient for energy  $E$  at position  $\mathbf{r}$ , and  $\sum_{n=1}^N \mu_n(E, \mathbf{r})$  corresponds to the summation of material attenuation at position  $\mathbf{r}$ .  $I_{m\ell}(E)$  represents the original x-ray photon intensity emitting from the x-ray source for energy  $E$ .

To simplify Eq. (1), we can separate the summation of x-ray attenuation coefficient  $\sum_{n=1}^N \mu_n(E, \mathbf{r})$  with a low-dimensional expansion. Here, we consider the basis material expansion

$$\sum_{n=1}^N \mu_n(E, \mathbf{r}) = \sum_{n=1}^N \phi_n(E) \rho_n(\mathbf{r}), \quad (2)$$

where  $\phi_n(E)$  is the mass-attenuation coefficient of the  $n^{\text{th}}$  material at energy  $E$  which can be determined by searching the tables in the national institute of standards and technology (NIST) report [34], and  $\rho_n(\mathbf{r})$  is the fraction of the  $n^{\text{th}}$  material component at location  $\mathbf{r}$ . In this work, we will focus on reconstructing  $\rho_n(\mathbf{r})$  which is referred to as material component maps. We denote the original x-ray photon flux as  $I_{m\ell}^{(0)}$  which can be expressed as

$$I_{m\ell}^{(0)} = \int_{E_m} I_{m\ell}(E) dE. \quad (3)$$

Substituting Eqs. (2) and (3) into Eq. (1), we have

$$S_{m\ell} = \int_{E_m} s_{m\ell}(E) e^{-\int_{r\in\ell} \sum_{n=1}^N \phi_n(E) \rho_n(\mathbf{r}) d\mathbf{r}} dE, \quad (4)$$

where  $S_{m\ell} = w_{m\ell} / I_{m\ell}^{(0)}$ , and  $s_{m\ell}(E)$  represents the normalized energy spectrum distribution of x-ray intensity and detector sensitivity

$$s_{m\ell}(E) = \frac{I_{m\ell}(E)}{I_{m\ell}^{(0)}}.$$

Considering the orders of integral and summation in the exponential function in Eq. (4) are exchangeable, there will be

$$S_{m\ell} = \int_{E_m} s_{m\ell}(E) e^{-\sum_{n=1}^N \phi_n(E) \int_{r \in \ell} \rho_n(\mathbf{r}) dr} dE. \quad (5)$$

Proceeding with a multi-energy CT model, we discretize Eq. (5) over the energy spectrum  $E_m$

$$\begin{aligned} S_{m\ell} &\approx \sum_i s_{m\ell}(E_i) e^{-\sum_{n=1}^N \phi_n(E_i) \int_{r \in \ell} \rho_n(\mathbf{r}) dr} \Delta E_i \\ &\approx \sum_i s_{m\ell}(E_i) e^{-\sum_{n=1}^N \phi_n(E_i) \mathbf{A}_{\ell\#} \mathbf{f}_n} \Delta E_i \\ &= \sum_i s_{m\ell}(E_i) e^{-\sum_{n=1}^N \phi_n(E_i) p_{n\ell}} \Delta E_i, \end{aligned} \quad (6)$$

where  $p_{n\ell} = \mathbf{A}_{\ell\#} \mathbf{f}_n = \int_{r \in \ell} \rho_n(\mathbf{r}) dr$ ,  $\mathbf{f}_n$  is the vectorization of the reconstructed  $n^{\text{th}}$  material map,  $\mathbf{A}$  presents projection matrix in  $\mathcal{R}^{L \times J}$  with  $J = J_1 \times J_2$ ,  $J_1$  and  $J_2$  represent width and height of the material maps,  $L$  is the number of total x-ray paths, and  $\mathbf{A}_{\ell\#}$  presents the  $\ell^{\text{th}}$  row of  $\mathbf{A}$ . Then, we perform a logarithm operation on both sides of Eq. (6) and obtain

$$\overline{q_{m\ell}} = \ln S_{m\ell} \approx \ln \left( \sum_i s_{m\ell}(E_i) e^{-\sum_{n=1}^N \phi_n(E_i) p_{n\ell}} \Delta E_i \right), \quad (7)$$

Because the summation locates inside of the logarithm operation, it is difficult to solve this problem. Inspired by the E-ART reconstruction algorithm for dual-energy CT [27], we unfold the right hand of Eq. (7) with the first-order of Taylor's expansion at the current point  $p_{n\ell}^{(k)}$

$$\begin{aligned} \overline{q_{m\ell}} &= \ln \left( \sum_i s_{m\ell}(E_i) e^{-\sum_{n=1}^N \phi_n(E_i) p_{n\ell}^{(k)}} \Delta E_i \right) - \\ &\sum_{n=1}^N \left( \frac{\left( \sum_i s_{m\ell}(E_i) \phi_n(E_i) e^{-\sum_{n=1}^N \phi_n(E_i) p_{n\ell}^{(k)}} \right)}{\left( \sum_i s_{m\ell}(E_i) e^{-\sum_{n=1}^N \phi_n(E_i) p_{n\ell}^{(k)}} \right)} (p_{n\ell} - p_{n\ell}^{(k)}) \right. \\ &\quad \left. + \mathcal{O}(p_{n\ell} - p_{n\ell}^{(k)}) \right), \end{aligned} \quad (8)$$

where  $\mathcal{O}(p_{n\ell} - p_{n\ell}^{(k)})$  presents Taylor's 2<sup>nd</sup> order infinitesimal and  $k$  indicates the current iteration step. Thus, Eq. (8) can be simplified as

$$\overline{q_{m\ell}} = q_{m\ell}^{(k)} - \sum_{n=1}^N \left( \frac{\Theta_{m\ell n}^{(k)}}{S_{m\ell}^{(k)}} (p_{n\ell} - p_{n\ell}^{(k)}) + \mathcal{O}(p_{n\ell} - p_{n\ell}^{(k)}) \right), \quad (9a)$$

where

$$q_{m\ell}^{(k)} = \ln \left( \sum_i s_{m\ell}(E_i) e^{-\sum_{n=1}^N \phi_n(E_i) p_{n\ell}^{(k)}} \Delta E_i \right), \quad (9b)$$

$$\Theta_{m\ell n}^{(k)} = \sum_i \phi_n(E_i) s_{m\ell}(E_i) \Delta E_i e^{-\sum_{n=1}^N \phi_n(E_i) p_{n\ell}^{(k)}}, \quad (9c)$$

$$S_{m\ell}^{(k)} = \sum_i s_{m\ell}(E_i) e^{-\sum_{n=1}^N \phi_n(E_i) p_{n\ell}^{(k)}}. \quad (9d)$$

Now, considering all energy channels, the vector form of Eq. (9a) can be expressed as

$$\begin{aligned} \begin{bmatrix} \overline{q_{1\ell}} - q_{1\ell}^{(k)} \\ \vdots \\ \overline{q_{M\ell}} - q_{M\ell}^{(k)} \end{bmatrix} &= - \begin{bmatrix} S_{1\ell}^{(k)} & \cdots & 0 \\ \vdots & \ddots & \vdots \\ 0 & \cdots & S_{M\ell}^{(k)} \end{bmatrix}^{-1} \times \\ &\quad \begin{bmatrix} \Theta_{1\ell 1}^{(k)} & \cdots & \Theta_{1\ell N}^{(k)} \\ \vdots & \ddots & \vdots \\ \Theta_{M\ell 1}^{(k)} & \cdots & \Theta_{M\ell N}^{(k)} \end{bmatrix} \begin{bmatrix} p_{1\ell} - p_{1\ell}^{(k)} \\ \vdots \\ p_{N\ell} - p_{N\ell}^{(k)} \end{bmatrix} + \begin{bmatrix} \sum_{n=1}^N \mathcal{O}(p_{n\ell} - p_{n\ell}^{(k)}) \\ \vdots \\ \sum_{n=1}^N \mathcal{O}(p_{n\ell} - p_{n\ell}^{(k)}) \end{bmatrix}. \end{aligned} \quad (10)$$

Eq. (10) is equivalent to

$$\begin{aligned} \begin{bmatrix} S_{1\ell}^{(k)} \sum_{n=1}^N \mathcal{O}(p_{n\ell} - p_{n\ell}^{(k)}) \\ \vdots \\ S_{M\ell}^{(k)} \sum_{n=1}^N \mathcal{O}(p_{n\ell} - p_{n\ell}^{(k)}) \end{bmatrix} &= \begin{bmatrix} S_{1\ell}^{(k)} & \cdots & 0 \\ \vdots & \ddots & \vdots \\ 0 & \cdots & S_{M\ell}^{(k)} \end{bmatrix} \begin{bmatrix} \overline{q_{1\ell}} - q_{1\ell}^{(k)} \\ \vdots \\ \overline{q_{M\ell}} - q_{M\ell}^{(k)} \end{bmatrix} \\ &+ \begin{bmatrix} \Theta_{1\ell 1}^{(k)} & \cdots & \Theta_{1\ell N}^{(k)} \\ \vdots & \ddots & \vdots \\ \Theta_{M\ell 1}^{(k)} & \cdots & \Theta_{M\ell N}^{(k)} \end{bmatrix} \begin{bmatrix} p_{1\ell} - p_{1\ell}^{(k)} \\ \vdots \\ p_{N\ell} - p_{N\ell}^{(k)} \end{bmatrix}, \end{aligned} \quad (11)$$

where  $S_{m\ell}^{(k)}$  ( $m = 1, \dots, M$ ) is a constant. To provide a better estimation for  $p_{n\ell}$  from the measurement  $\overline{q_{m\ell}}$  based on Eq. (8), we need to minimize the error term which is equivalent to the right side of Eq. (11). That is,

$$\min_{\mathbf{P}} \left\{ \sum_{\ell=1}^L \left\| \Theta_{\#\ell\#}^{(k)} (\mathbf{P}_{\#\ell} - \mathbf{P}_{\#\ell}^{(k)}) + \mathbf{S}_{\ell}^{(k)} (\overline{\mathbf{Q}}_{\#\ell} - \mathbf{Q}_{\#\ell}^{(k)}) \right\|_F^2 \right\}, \quad (12)$$

where  $\mathbf{P}_{\#\ell}$  is  $\ell^{\text{th}}$  column of  $\mathbf{P} = \begin{bmatrix} p_{11} & \cdots & p_{1L} \\ \vdots & \ddots & \vdots \\ p_{N1} & \cdots & p_{NL} \end{bmatrix}$  and represents the measured projection data over the full energy spectrum for the  $\ell^{\text{th}}$  x-ray path,  $\Theta_{\#\ell\#}^{(k)} = \begin{bmatrix} \Theta_{1\ell 1}^{(k)} & \cdots & \Theta_{1\ell N}^{(k)} \\ \vdots & \ddots & \vdots \\ \Theta_{M\ell 1}^{(k)} & \cdots & \Theta_{M\ell N}^{(k)} \end{bmatrix}$ ,  $\mathbf{S}_{\ell}^{(k)} = \begin{bmatrix} S_{1\ell}^{(k)} & \cdots & 0 \\ \vdots & \ddots & \vdots \\ 0 & \cdots & S_{M\ell}^{(k)} \end{bmatrix}$ ,  $\overline{\mathbf{Q}}_{\#\ell} = \begin{bmatrix} \overline{q_{1\ell}} \\ \vdots \\ \overline{q_{M\ell}} \end{bmatrix}$  and  $\mathbf{Q}_{\#\ell}^{(k)} = \begin{bmatrix} q_{1\ell}^{(k)} \\ \vdots \\ q_{M\ell}^{(k)} \end{bmatrix}$ .

Substituting  $p_{n\ell} = \mathbf{A}_{\ell\#} \mathbf{f}_n$  into Eq. (12), we have

$$\min_{\mathcal{F}} \left\{ \sum_{\ell=1}^L \left\| \Theta_{\#\ell\#}^{(k)} ((\mathbf{A}_{\ell\#} \mathcal{F})^T - (\mathbf{A}_{\ell\#} \mathcal{F}^{(k)})^T) + \mathbf{S}_{\ell}^{(k)} (\overline{\mathbf{Q}}_{\#\ell} - \mathbf{Q}_{\#\ell}^{(k)}) \right\|_F^2 \right\}, \quad (13)$$

where  $\mathcal{F} = [\mathbf{f}_1, \mathbf{f}_2, \dots, \mathbf{f}_N]$ , and  $\mathcal{F}^{(k)}$  represents the material component maps at the  $k^{\text{th}}$  iteration. Eq. (13) can be directly used to reconstruct material maps, and it can be considered as a material reconstruction model. To solve the optimization problem of Eq. (13), we employ the constraint  $\mathbf{P} = (\mathbf{A}\mathcal{F})^T$ ,

$$\min_{\mathcal{F}} \left\{ \sum_{\ell=1}^L \left\| \Theta_{\#\ell\#}^{(k)} (\mathbf{P}_{\#\ell} - \mathbf{P}_{\#\ell}^{(k)}) + \mathbf{S}_{\ell}^{(k)} (\overline{\mathbf{Q}}_{\#\ell} - \mathbf{Q}_{\#\ell}^{(k)}) \right\|_F^2 \right\}, \quad (14)$$

s. t.  $\mathbf{P} = (\mathbf{A}\mathcal{F})^T$ .

Eq. (14) is a constrained optimization problem, and it can be converted into an unconstrained one

$$\min_{\mathcal{F}, \mathbf{P}} \left\{ \sum_{\ell=1}^L \left\| \boldsymbol{\Theta}_{\#\ell\#}^{(k)} (\mathbf{P}_{\#\ell} - \mathbf{P}_{\#\ell}^{(k)}) + \mathbf{S}_{\ell}^{(k)} (\bar{\mathbf{Q}}_{\#\ell} - \mathbf{Q}_{\#\ell}^{(k)}) \right\|_F^2 + \lambda \left\| (\mathbf{A}\mathcal{F})^T - \mathbf{P} \right\|_F^2 \right\}, \quad (15)$$

where  $\lambda > 0$  is a constant to balance the two terms. Eq. (15) is equal to solving the following two sub-problems:

$$\left\{ \min_{\mathbf{P}} \left\{ \sum_{\ell=1}^L \left\| \boldsymbol{\Theta}_{\#\ell\#}^{(k)} (\mathbf{P}_{\#\ell} - \mathbf{P}_{\#\ell}^{(k)}) + \mathbf{S}_{\ell}^{(k)} (\bar{\mathbf{Q}}_{\#\ell} - \mathbf{Q}_{\#\ell}^{(k)}) \right\|_F^2 + \lambda \left\| ((\mathbf{A}\mathcal{F})^T)^{(k)} - \mathbf{P} \right\|_F^2 \right\} \right. \quad (16a)$$

$$\left. \min_{\mathcal{F}} \left\| (\mathbf{A}\mathcal{F})^T - \mathbf{P}^{(k+1)} \right\|_F^2. \quad (16b) \right.$$

The goal of Eq. (16a) is to decompose the measured projection dataset to all material components, which can be considered as a projection decomposition model. To solve Eq. (16a), let us denote

$$\mathbf{Y}(\mathbf{P}) = \left\{ \sum_{\ell=1}^L \left\| \boldsymbol{\Theta}_{\#\ell\#}^{(k)} (\mathbf{P}_{\#\ell} - \mathbf{P}_{\#\ell}^{(k)}) + \mathbf{S}_{\ell}^{(k)} (\bar{\mathbf{Q}}_{\#\ell} - \mathbf{Q}_{\#\ell}^{(k)}) \right\|_F^2 + \lambda \left\| ((\mathbf{A}\mathcal{F})^T)^{(k)} - \mathbf{P} \right\|_F^2 \right\}. \quad (17)$$

According to the *Theorem 1* in the Appendix A.I,  $\mathbf{Y}(\mathbf{P})$  can be minimized in the following iterative format

$$\left( \mathbf{P}_{\#1}^{(k+1)}, \dots, \mathbf{P}_{\#L}^{(k+1)} \right) = \begin{pmatrix} \mathbf{P}_{\#1}^{(k)} - \beta_1 \left( \boldsymbol{\Theta}_{\#1\#}^{(k)T} \boldsymbol{\Theta}_{\#1\#}^{(k)} + \lambda \mathbf{J} \right)^{-1} \mathbf{S}_1^{(k)} (\bar{\mathbf{Q}}_{\#1} - \mathbf{Q}_{\#1}^{(k)}) \\ \vdots \\ \mathbf{P}_{\#L}^{(k)} - \beta_1 \left( \boldsymbol{\Theta}_{\#L\#}^{(k)T} \boldsymbol{\Theta}_{\#L\#}^{(k)} + \lambda \mathbf{J} \right)^{-1} \mathbf{S}_L^{(k)} (\bar{\mathbf{Q}}_{\#L} - \mathbf{Q}_{\#L}^{(k)}) \end{pmatrix}^T, \quad (18)$$

where  $\beta_1$  and  $\lambda$  are constant parameters, and  $\mathbf{J}$  is an identity transform. Particularly,  $\mathbf{P}_{\#\ell}^{(k+1)}$  can be updated as

$$\mathbf{P}_{\#\ell}^{(k+1)} = \mathbf{P}_{\#\ell}^{(k)} - \beta_1 \left( \boldsymbol{\Theta}_{\#\ell\#}^{(k)T} \boldsymbol{\Theta}_{\#\ell\#}^{(k)} + \lambda \mathbf{J} \right)^{-1} \mathbf{S}_{\ell}^{(k)} (\bar{\mathbf{Q}}_{\#\ell} - \mathbf{Q}_{\#\ell}^{(k)}). \quad (19)$$

Now, we consider Eq. (16b), which is equivalent to

$$\min_{\mathcal{F}} \left\| \mathbf{A}\mathcal{F} - (\mathbf{P}^{(k+1)})^T \right\|_F^2. \quad (20)$$

Eq. (20) can be viewed as a material map reconstruction model. Note that Eq. (20) is a convex quadratic optimization, it can be solved by the steepest descent method

$$\mathcal{F}^{(k+1)} = \mathcal{F}^{(k)} - \beta_2 \mathbf{A}^T \left( \mathbf{A}\mathcal{F}^{(k)} - (\mathbf{P}^{(k+1)})^T \right), \quad (21)$$

Where  $\beta_2$  is a relaxation factor in (0,2). If the projections are sufficient, we can also employ the classical analytic reconstruction methods to directly solve Eq. (20).

From Eqs. (19) and (21), we can observe that the proposed material reconstruction algorithm can be divided into projection data decomposition and map reconstruction procedures. Because this algorithm can directly reconstruct the material maps instead of decomposing the reconstructed spectral image, we name it material simultaneous algebraic reconstruction technique (MSART). The major steps of the proposed MSART can be summarized as the following Algorithm I.

---

### Algorithm I: MSART

---

**Input:**  $\bar{\mathbf{Q}}$ ; Normalized energy spectrum;  $\beta_1$ ;  $\beta_2$ ;  $\lambda$ ;

1: Initialization:  $\mathcal{F} \leftarrow \mathbf{0}$ ,  $\mathbf{Q}^{(0)} \leftarrow \mathbf{0}$ ,  $\mathbf{P} \leftarrow \mathbf{0}$ ;  $k = 1$ ;

2: **Repeat**

**Part I: Projection decomposition**

3: **for**  $\ell := 1, 2, \dots, L$  **do**

4: **for**  $m := 1, 2, \dots, M$  **do**

5:  $\boldsymbol{\Theta}_{m\ell n}^{(k)} = \sum_i \left( \phi_n(E_i) s_{m\ell}(E_i) e^{-\sum_{n=1}^N \phi_n(E_i) p_{n\ell}^{(k)}} \right)$ ;

6:  $s_{m\ell}^{(k)} = \sum_i \left( s_{m\ell}(E_i) e^{-\sum_{n=1}^N \phi_n(E_i) p_{n\ell}^{(k)}} \right)$ ;

7:  $q_{m\ell}^{(k)} = \ln \left( \sum_i s_{m\ell}(E_i) e^{-\sum_{n=1}^N \phi_n(E_i) p_{n\ell}^{(k)}} \Delta E_i \right)$ ;

8: **end for**

9:  $\mathbf{P}_{\#\ell}^{(k+1)} = \mathbf{P}_{\#\ell}^{(k)} - \beta_1 \left( (\boldsymbol{\Theta}_{\#\ell\#}^{(k)T} \boldsymbol{\Theta}_{\#\ell\#}^{(k)} + \lambda \mathbf{J})^{-1} \mathbf{S}_{\ell}^{(k)} (\bar{\mathbf{Q}}_{\#\ell} - \mathbf{Q}_{\#\ell}^{(k)}) \right)$ ;

10: **end for**

**Part II: Material image reconstruction**

11:  $\mathcal{F}^{(k+1)} = \mathcal{F}^{(k)} - \beta_2 \mathbf{A}^T \left( \mathbf{A}\mathcal{F}^{(k)} - (\mathbf{P}^{(k+1)})^T \right)$ ;

12:  $k = k + 1$ ;

13: Enforcing the positive constraint over  $\mathcal{F}^{(k+1)}$ ;

14: **Until** convergence

**Output:** Material component map  $\mathcal{F}$

---

## III. BLOCK MATCHING FRAME MATERIAL RECONSTRUCTION (BMFMR) METHOD

### A. Block Matching Filtering Frame

The BM3D was proposed in [30] as a nonlocal image denoising tool based on adaptive high-order groupwise models. For better understanding of the BM3D model, we first review the BM3D flowchart, which can be divided into three steps: i) *Grouping by Matching*. Similar small blocks in a given image window are collected to form a group. These Blocks in each group are stacked together to build 3D data arrays. ii) *Collaborative hard-threshold filtering*. The noise in 3D data arrays are suppressed by a hard-threshold filtering on the groupwise spectrum coefficients in a transform domain. The invertible transform is performed on spectral coefficients to estimate all the grouped blocks, and then the estimated blocks are re-arranged into the original image positions. iii) *Aggregation*. The final image is obtained by weighting all blockwise estimations. The theorem of BM3D frame based matrix representation was introduced in [31]. Assuming there is a vectorized image  $\in \mathcal{R}^J$ , the analysis equation for the BM3D image model can be formulated as

$$\mathbf{W} = \Phi(\mathbf{y}). \quad (22)$$

Here,  $\mathbf{W} \in \mathcal{R}^B$  is the 3D groupwise spectrum to store the 3D transform domain coefficients for each group extracted from the image.  $\Phi \in \mathcal{R}^{B \times J}$  ( $B \gg J$ ) represents a frame, which transforms the image  $\mathbf{y}$  into groupwise spectrum space and provides an explicit expression of the BM3D analysis operation. The inverse transform matrix, which converts the groupwise spectrum coefficients into the image space, can be considered as another transform frame. Moreover, it can be implemented by a frame  $\Psi \in \mathcal{R}^{J \times B}$  and thus the original signal can be recovered by

$$\mathbf{y} = \Psi(\mathbf{W}). \quad (23)$$

The product  $\Phi\Psi$  should be  $\mathbf{I}_{B \times B}$ . Both  $\Phi$  and  $\Psi$  mean operating the particular 3D transform on each extracted group. The 3D transform form can be chosen such that it can be divided into a pair of 2D-intrablock and 1D-interblock sub-transforms. These separable transforms can not only efficiently exploit the data structure of the 3D patch-based

groups, but also greatly reduce the computational complexity compared to a non-separable transform. For more details, refer to [31].

### B. Algorithm model

Although the BM3D frame was originally proposed for image denoising and deblurring [31], it has been widely applied for other applications. For example, the BM3D was introduced to MRI reconstruction and obtained satisfied results compared with other competing methods [33]. Considering the similarity of nonlocal structures from each material component map, we introduce the BM3D frame into the MSART model to enhance the anti-noising ability, leading to the BMFMR algorithm. Based on Eq. (13), the BMFMR can be modeled as

$$\min_{\mathcal{F}} \left\{ \sum_{\ell=1}^L \left\| \Theta_{\#\ell\#}^{(k)} ((\mathbf{A}_{\ell\#}\mathcal{F})^T - ((\mathbf{A}_{\ell\#}\mathcal{F})^T)^{(k)}) + \mathbf{S}_{\ell}^{(k)} (\bar{\mathbf{Q}}_{\#\ell} - \mathbf{Q}_{\#\ell}^{(k)}) \right\|_F^2 + \sum_{n=1}^N \kappa_n \|\Phi_n(\mathbf{f}_n)\|_p \right\}, \quad (24)$$

where  $\|\cdot\|_p$  represents the  $p$ -norm ( $0 \leq p \leq 1$ ),  $\kappa$  represents the regularization vector and  $\kappa_n$  represents the regularization parameter of  $n^{\text{th}}$  material reconstruction. In this work, we only consider the case  $p = 0$ , and  $\kappa_n$  is selected as a constant vector. The solution of Eq. (24) can be obtained by adopting a similar procedure of Eq. (13) except for the material map reconstruction step. That is, Eq. (24) can be converted into two sub-problems

$$\min_{\mathbf{P}} \left\{ \sum_{\ell=1}^L \left\| \Theta_{\#\ell\#}^{(k)} (\mathbf{P}_{\#\ell} - \mathbf{P}_{\#\ell}^{(k)}) + \mathbf{S}_{\ell}^{(k)} (\bar{\mathbf{Q}}_{\#\ell} - \mathbf{Q}_{\#\ell}^{(k)}) \right\|_F^2 + \lambda \left\| ((\mathbf{A}\mathcal{F})^T)^{(k)} - \mathbf{P} \right\|_F^2 \right\}, \quad (25a)$$

$$\min_{\mathcal{F}} \left\{ \left\| \mathbf{A}\mathcal{F} - (\mathbf{P}^{(k+1)})^T \right\|_F^2 + \sum_{n=1}^N \tau_n \|\Phi_n(\mathbf{f}_n)\|_0 \right\}. \quad (25b)$$

where  $\tau_n = \kappa_n/\lambda$  and  $\tau$  can be expressed as  $\kappa/\lambda$ . Eq. (25a) is exactly the same as Eq. (16a), which has been solved in the previous section. Eq. (25b) contains the  $L_0$ -norm of 3D transform domain coefficients and it is an NP hard problem. Here, we introduce an auxiliary matrix  $\mathbf{g}_n \in \mathcal{R}^{J_1 \times J_2}$ , which is a cell of the 3<sup>rd</sup> tensor  $\mathcal{G}$ . Then, Eq. (25b) can be read as

$$\min_{\mathbf{f}_n} \left\| \mathbf{A}\mathbf{f}_n - (\mathbf{P}_{n\#}^{(k+1)})^T \right\|_F^2 + \tau_n \|\Phi_n(\mathbf{g}_n)\|_0, \text{ s. t. } \mathbf{g}_n = \mathbf{f}_n. \quad (27)$$

Now, Eq. (27) is a linear optimization problem with equality constraints. This can be further converted into an unconstrained linear optimization problem:

$$\min_{\mathbf{f}_n, \mathbf{g}_n, \mathbf{t}_n} \left( \left\| \mathbf{A}\mathbf{f}_n - (\mathbf{P}_{n\#}^{(k+1)})^T \right\|_F^2 + \gamma_n \|\mathbf{f}_n - \mathbf{g}_n - \mathbf{t}_n\|_F^2 + \tau_n \|\Phi_n(\mathbf{g}_n)\|_0 \right). \quad (28)$$

Here,  $\mathbf{t}_n \in \mathcal{R}^{J_1 \times J_2}$  represents a cell of the 3<sup>rd</sup> error-feedback tensor  $\mathcal{T}$ , and  $\gamma_n$  is the coupling parameter of  $n^{\text{th}}$  material component between the data fidelity and difference terms. Because Eq. (28) contains three variable matrixes, it can be further divided into three steps using an alternating iterative strategy:

$$\min_{\mathbf{f}_n} \left\| \mathbf{A}\mathbf{f}_n - (\mathbf{P}_{n\#}^{(k+1)})^T \right\|_F^2 + \gamma_n \|\mathbf{f}_n - \mathbf{g}_n^{(k)} - \mathbf{t}_n^{(k)}\|_F^2, \quad (29a)$$

$$\min_{\mathbf{g}_n} \left\| \mathbf{f}_n^{(k+1)} - \mathbf{g}_n - \mathbf{t}_n^{(k)} \right\|_F^2 + \tau_n \|\Phi_n(\mathbf{g}_n)\|_0, \quad (29b)$$

$$\min_{\mathbf{t}_n} \left\| \mathbf{f}_n^{(k+1)} - \mathbf{g}_n^{(k+1)} - \mathbf{t}_n \right\|_F^2. \quad (29c)$$

Because Eqs. (29a) and (29c) are convex quadratic optimization problems, their solution can be given by Eqs. (30) and (31),

$$\mathbf{f}_n^{(k+1)} = \mathbf{f}_n^{(k)} - \beta_2 \mathbf{A}^T (\mathbf{A}\mathbf{f}_n^{(k)} - (\mathbf{P}_{n\#}^{(k+1)})^T) - \gamma_n (\mathbf{f}_n^{(k)} - \mathbf{g}_n^{(k)} - \mathbf{t}_n^{(k)}), \quad (30)$$

$$\mathbf{t}_n^{(k+1)} = \mathbf{t}_n^{(k)} - (\mathbf{f}_n^{(k+1)} - \mathbf{g}_n^{(k+1)}). \quad (31)$$

Eq. (29b) is to update  $\mathbf{g}_n$  with respect to fixed  $\mathbf{f}_n^{(k+1)}$  and  $\mathbf{t}_n^{(k)}$ , which can be treated as a denoising problem with an attenuation operation over the frame  $\Phi_n$ . Because Eq. (29b) contains the  $L_0$ -norm of 3D transform domain coefficients, a hard thresholding method is employed. Thus, the update of  $\mathbf{g}_n$  can be given as

$$\mathbf{g}_n^{(k+1)} = \Psi_n [\Phi_n(\mathbf{f}_n^{(k+1)} - \mathbf{t}_n^{(k)})]_{\tau_n}, \quad (32)$$

where the operator  $[\cdot]_{\tau_n}$  denotes the hard thresholding operation, which can be calculated as follow [35]

$$[\Phi_n(\mathbf{f}_n^{(k+1)} - \mathbf{t}_n^{(k)})]_{\tau_n} = \begin{cases} 0, & \Phi_n(\mathbf{f}_n^{(k+1)} - \mathbf{t}_n^{(k)}) < \sqrt{\tau_n} \\ \Phi_n(\mathbf{f}_n^{(k+1)} - \mathbf{t}_n^{(k)}), & \Phi_n(\mathbf{f}_n^{(k+1)} - \mathbf{t}_n^{(k)}) \geq \sqrt{\tau_n} \end{cases}. \quad (33)$$

In fact, Eq. (33) can be simply treated as the BM3D denoising algorithm formulated by the frame notations [31]. For the proposed BMFMR technique, we utilize the shrinkage method Eq. (32) as an approximate solution for (29b).

### C. Algorithm comparison

To demonstrate the advantages of BMF regularization term in image reconstruction, the total variation (TV) and non-local mean (NLM) regularizations are introduced into the model Eq. (13). As a result, we formulate TV based and NLM based material reconstruction methods, named as TVMR and NLMR. The mathematic model of TVMR can be written as

$$\min_{\mathcal{F}} \left\{ \sum_{\ell=1}^L \left\| \Theta_{\#\ell\#}^{(k)} ((\mathbf{A}_{\ell\#}\mathcal{F})^T - ((\mathbf{A}_{\ell\#}\mathcal{F})^T)^{(k)}) + \mathbf{S}_{\ell}^{(k)} (\bar{\mathbf{Q}}_{\#\ell} - \mathbf{Q}_{\#\ell}^{(k)}) \right\|_F^2 + \sum_{n=1}^N \xi_n \text{TV}(\mathbf{f}_n) \right\}, \quad (34)$$

where  $\xi_n$  is an element of vector  $\xi$  and it represents the regularization parameter of the  $n^{\text{th}}$  material reconstruction. To solve Eq. (34), we adopt the same procedure of BMFMR except for the material map reconstruction step. For the material map reconstruction, a similar strategy reported in [36] is employed.

### D. Algorithm implementation details

The BMFMR method can be divided into two main procedures: projection decomposition and image reconstruction. Because the projection decomposition steps in BMFMR, NLMR and TVMR are the same as the MSART method, we only summarized the material image reconstruction steps. The workflow of the BMFMR algorithm



is summarized as Algorithm II. First, the projection data from different energy channels are decomposed into different material projection datasets. Then, each material map can be obtained from the corresponding material projection. Because different material components have different levels of noise, parameters should be optimized and selected to reconstruct different materials. The steps 11-16 are to reconstruct the material maps one by one. Regarding the update of step 12, the projection matrix  $\mathbf{A}$  is too large to calculate directly. Thus, it is necessary to divide it into two substeps:

$$\mathbf{f}_n^{(k+\frac{1}{2})} = \mathbf{f}_n^{(k)} - \beta_2 \mathbf{A}^T (\mathbf{A} \mathbf{f}_n^{(k)} - (\mathbf{P}_{n\#}^{(k+1)})^T), \quad (35)$$

$$\mathbf{f}_n^{(k+1)} = \mathbf{f}_n^{(k+\frac{1}{2})} - \gamma_n (\mathbf{f}_n^{(k)} - \mathbf{g}_n^{(k)} - \mathbf{t}_n^{(k)}), \quad (36)$$

where  $\mathbf{f}_n^{(k+\frac{1}{2})}$  stands for the intermediate result. First, we calculate  $\mathbf{f}_n^{(k)} - \mathbf{g}_n^{(k)} - \mathbf{t}_n^{(k)}$  and store it. Then,  $\mathbf{f}_n^{(k+\frac{1}{2})}$  can be updated by using Eq. (35). Finally,  $\mathbf{f}_n^{(k+1)}$  can be calculated according to Eq. (36). The steps 13–14 are the BM3D hard thresholding denoising process for the current estimation. These hard thresholding steps can be implemented by using a highly available online optimized BM3D denoising toolbox [29]. However, we only employ the 3D transform shrinkage step and avoid the wiener collaborative step in the BM3D denoising filtering. To accurately generate the two frames  $\Psi_n$  and  $\Phi_n$  for the  $n^{\text{th}}$  material reconstruction, the noise level  $\sigma$  is estimated from the current map. Because different material images correspond to different noise levels, different thresholds  $\tau_n$  can effectively improve the denoising ability for Algorithm II. In our all experiments, except the hard thresholding coefficient column vector  $\boldsymbol{\tau}$ , other parameters are the same as the openly available BM3D denoising toolbox.

#### Algorithm II: BMFMR

**Input:**  $\bar{Q}$ ; Normalized energy spectrum;  $\beta_1$ ;  $\beta_2$ ;  $\lambda$ ;  $\gamma$ ;  $\boldsymbol{\tau}$ ;  
1: Initialization:  $\mathcal{F} \leftarrow \mathbf{0}$ ,  $Q^{(0)} \leftarrow \mathbf{0}$ ,  $P \leftarrow \mathbf{0}$ ;  $k \leftarrow 0$ ;  $\mathcal{T} \leftarrow \mathbf{0}$ ;  $\mathcal{G} \leftarrow \mathbf{0}$ ;  
2: **Repeat**  
**Part I: Projection decomposition**  
**Part II: Material image reconstruction**  
11: **for**  $n = 1, 2, \dots, N$  **do**  
12:  $\mathbf{f}_n^{(k+1)} = \mathbf{f}_n^k - \beta_2 \mathbf{A}^T (\mathbf{A} \mathbf{f}_n^{(k)} - (\mathbf{P}_{n\#}^{(k+1)})^T) - \gamma_n (\mathbf{f}_n^{(k)} - \mathbf{g}_n^{(k)} - \mathbf{t}_n^{(k)})$ ;  
13: Generating two frames  $\Psi_n$  and  $\Phi_n$  using  $\mathbf{f}_n^{(k+1)} - \mathbf{t}_n^{(k)}$ ;  
14:  $\mathbf{g}_n^{(k+1)} = \Psi[\Phi(\mathbf{f}_n^{(k+1)} - \mathbf{t}_n^{(k)})]_{\tau_n}$ ;  
15:  $\mathbf{t}_n^{(k+1)} = \mathbf{t}_n^{(k)} - (\mathbf{f}_n^{(k)} - \mathbf{g}_n^{(k+1)})$ ;  
16: **end for**  
17: Enforcing the positive constraint over  $\mathcal{F}^{(k+1)}$ ;  
18:  $k = k + 1$ ;  
19: **Until** convergence  
**Output:** Material component map  $\mathcal{F}$

## IV. EXPERIMENTS AND RESULTS

In this study, we first perform extensive numerical simulations to validate the correctness of our theory and the proposed algorithms. Then, physical phantom experiments are carried out to demonstrate their applications. The advantages of BMFMR method in terms of material map reconstruction are shown by comparing with the MSART, TVMR and NLMMR methods. To quantitatively evaluate the performance of all material reconstruction methods, the root means square

error (RMSE), peak-signal-to-noise ratio (PSNR) and structural similarity (SSIM) are calculated.

### A. Numerical Simulations

#### A.1). Experiment preparation

A realistic mouse thorax phantom, containing three basic material: bone, soft tissue and iodine (Fig. 1), is utilized in this study. As shown in Fig. 1, 1.2% iodine is introduced as a contrast agent. A polychromatic 50KVp x-ray source is employed. Fig. 2(a) illustrates the corresponding normalized x-ray spectrum for this study. 341 uniform samples (from 16 KeV to 50 KeV) are extracted and divided into eight different energy channels: [16, 22) keV, [22, 25) keV, [25, 28) keV, [28, 31) keV, [31, 34) keV, [34, 37) keV, [37, 41) keV, [41, 50) keV. To evaluate the proposed algorithms, the attenuation curves of basic materials are given in Fig. 2(b). From Fig. 2(b), we can observe that there is only one k-edge among the material attenuation curves around 33.7 KeV for iodine. As for the scan geometry, the distances from source to PCD and rotation center are 180mm and 132mm, respectively. The PCD contains 512 detector cells, each of which covers a length of 0.1mm. 640 projections are uniformly collected over a full scan. To simulate Poisson noise, the photon numbers of each x-ray path are set as  $10^5$ . The higher the photon number is, the lower the noise level is. The noisy projection datasets in Radon space are obtained by a post-logarithmic operation on the received photon numbers. All the reconstructed material component images are  $512 \times 512$  matrixes, and each pixel covers an area of  $0.075 \times 0.075$  mm<sup>2</sup>. All the iterative algorithms are stopped after 40 iterations.



Fig.1 Three basic material maps of the realistic mouse thorax phantom. (a), (b) and (c) are bone, water and iodine material maps, respectively. The display windows for (a), (b) and (c) are [0 1], [0 1] and [0 0.012], respectively.

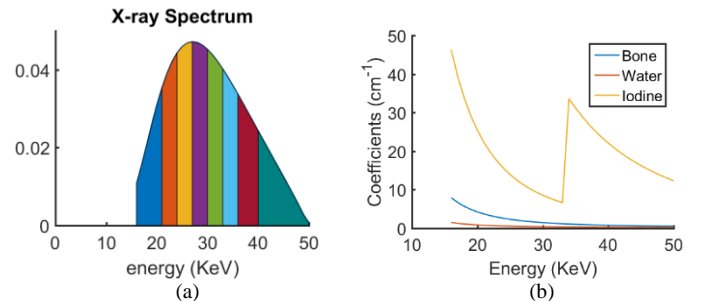


Fig.2 Normalized spectrum of a 50 kV x-ray source used for CT simulation (left) and material-attenuation curves of three different basis materials (right).

Table 1. Material image reconstruction parameters.

Numerical Simulation	Bone			Water			Iodine		
	$\tau_1$	$\sigma_1$	$\gamma_1$	$\tau_2$	$\sigma_2$	$\gamma_2$	$\tau_3$	$\sigma_3$	$\gamma_3$
	0.1	35	0.03	0.01	35	0.6	0.05	3	0.001
Physical Experiments	Aluminum			Water			Iodine		
	$\tau_1$	$\sigma_1$	$\gamma_1$	$\tau_2$	$\sigma_2$	$\gamma_2$	$\tau_3$	$\sigma_3$	$\gamma_3$
	0.8	35	0.2	0.6	25	0.2	0.004	3	0.02

The parameter selection is a challenging problem for iterative image reconstruction algorithms. In this study, both  $\beta_1$  and  $\beta_2$  are relaxation factors and they are set as 0.2. The Lagrangian multiplier  $\lambda$  is fixed as 0.002 in all the algorithms. To make it clear for the parameter selection of all the algorithms, other parameters are summarized in table 1.

## A.2). Reconstruction results

### a). Material reconstruction

Fig. 3 shows three basis material reconstructions. From Fig. 3, on one hand, we can observe that the proposed algorithms can reconstruct material maps directly from projection datasets, validating the correctness of our theoretical results. On the other hand, the BMFMR method obtains the best image quality compared with the MSART, TVMR and NLMMR algorithms. Because we decompose the projections into different material components, the noise levels can be easily magnified, resulting in magnified artifacts in the reconstructed material maps. Fortunately, these artifacts can be effectively reduced by certain prior regularization information, such as TV, NLM or BMF. However, the images are blocky and some edge information is lost in the results of TV regularization. As for the NLMMR results, the bony edge indicated by arrows in the 3<sup>rd</sup> row of Fig. 3 are blurry. Interestingly, the BMFMR algorithm can well preserve the edge information and recover clear structures, which can be observed by the magnified regions of bone and water materials in Fig. 3. Regarding the color rendering images, the magnified regions marked with ‘‘C’’ further confirm the outstanding performance of the BMFMR method in terms of image edge preservation.

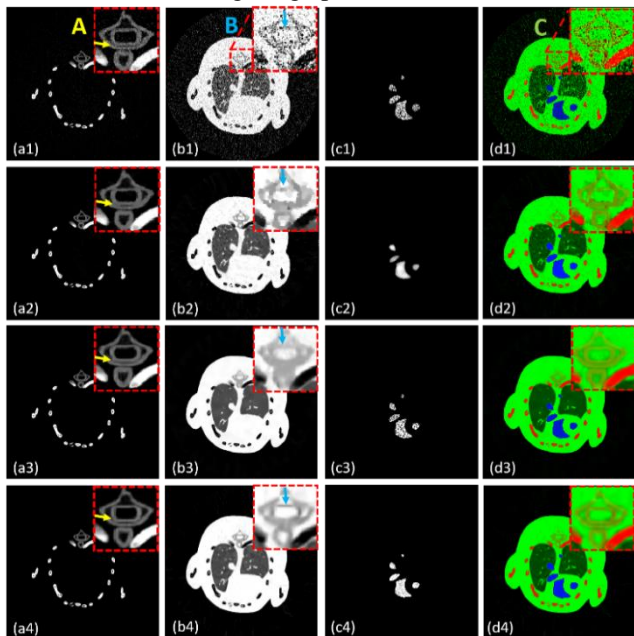


Fig. 3 Reconstructed basis material images from 640 projections with  $10^6$  photons for each x-ray path. The 1<sup>st</sup> to 3<sup>rd</sup> column images are the reconstructed maps of bone, water and iodine, where the display windows are [0 1], [0 1] and [0.011 0.012]. The 4<sup>th</sup> column is the merged color image. The 1<sup>st</sup> to 4<sup>th</sup> rows are reconstructed by the MSART, TVMR, NLMMR and BMFMR methods, respectively.

To further demonstrate the advantages of the BMFMR method in material decomposition, in Fig. 4 we show the reconstructed difference images with respect to the ground

truths. From Fig. 4, one can see the MSART reconstructions are strongly affected by noise. The TVMR reduces the artifacts, but the profiles of iodine are clearer. Compared with the NLMMR, the results from BMFMR are closer to the ground truths, and it is more obvious in the bone and iodine maps. To quantitatively evaluate the accuracy of material reconstruction of all algorithms, we compute the RMSE, SSIM and PSNR as listed in table 2. One can see that the BMFMR method has the smallest RMSEs in all material reconstruction (bone, water and iodine) for different photon numbers, followed by the NLMMR method which has smaller RMSEs than the MSART algorithm. For the index of SSIM, which usually measures the similarity between two images, the material component maps from the BMFMR almost always have higher similarity with respect to the ground truths. Regarding the PSNR, the proposed BMFMR algorithm can obtain higher values. All of these quantitative results further confirm the advantages of our proposed BMFMR algorithm.

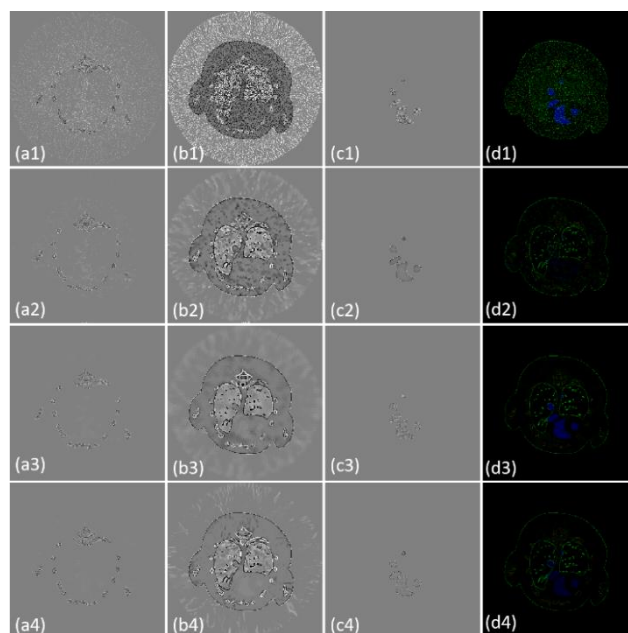


Fig. 4 Same as Fig.3 but the difference images with respect to the ground truths without magnified ROIs. From the 1st to 3rd columns, the display windows are [-0.2, 0.2], [-0.2, 0.2] and [-0.001, 0.001], respectively.

Table 2. Quantitative evaluation results of different reconstruction methods.

Material	Index	MSART	TVMR	NLMMR	BMFMR
Bone	RMSE( $10^{-2}$ )	1.43	1.37	<b>1.32</b>	<b>1.32</b>
	SSIM	0.5839	0.9520	0.9785	<b>0.9870</b>
	PSNR	31.50	37.29	37.58	<b>37.61</b>
Water	RMSE( $10^{-2}$ )	6.43	6.26	5.87	<b>5.86</b>
	SSIM	0.330	0.709	0.768	<b>0.8490</b>
	PSNR	16.43	24.06	24.63	<b>24.64</b>
Iodine	RMSE( $10^{-2}$ )	2.35	1.77	1.69	<b>1.62</b>
	SSIM	0.9882	<b>0.9991</b>	0.9941	0.9980
	PSNR	70.43	75.03	75.42	<b>75.80</b>

### b). Parameters analysis

The parameters of BMFMR mainly include a pair of relaxation factors ( $\beta_1, \beta_2$ ), two regularization factors ( $\lambda, \gamma$ ) and one hard-threshold vector  $\tau$  and the noise estimation vector  $\sigma$ . Regarding the relaxation pair ( $\beta_1, \beta_2$ ), both of them are set as 0.2 in this study [36].  $\lambda$  is to balance the data fidelity and regularization terms, and it depends on the

material composition. Similarly,  $\boldsymbol{\gamma}$  is also to balance the data fidelity and regularization terms. Regarding the hard-threshold vector  $\boldsymbol{\tau}$ , it can be determined by the noise level of the corresponding material component. In this study,  $\lambda$  is fixed as a constant and  $\boldsymbol{\gamma}$  is set as a constant vector. To investigate the performance of the BMFMR algorithm with respect to different parameters, we quantitatively analyze the image quality of water with full-scan in the case of  $10^5$  photons by relaxing one or two free parameters and fixing others. In this part, all algorithms are stopped after 40 iterations, and the RMSE and PSNR are computed for analysis.

**Regularization parameters ( $\lambda$ ,  $\boldsymbol{\gamma}$ ):** As aforementioned,  $\boldsymbol{\gamma}$  is set as a constant vector. Fig. 5(a) shows the quantitative results with respect to different constants for  $\boldsymbol{\gamma}$ . We can see that an appropriate value of  $\boldsymbol{\gamma}_2$  (i.e.,  $\boldsymbol{\gamma}_2=0.6$ ) can obtain satisfied quantitative results. Regarding the parameter  $\lambda$ , it is to balance the decomposed projection and image reconstruction terms. Fig.5 (b) shows the quantitative results with respect to different  $\lambda$  values. It implies a greater  $\lambda$  may compromise image quality. On the other hand, according to the Theorem 1 in the appendix A.1., a greater value of  $\lambda$  may improve the stability of  $(\boldsymbol{\theta}_{\#\#\#}^{(k)T} \boldsymbol{\theta}_{\#\#\#}^{(k)} + \lambda \mathbf{J})^{-1}$ . Therefore, after balancing these two factors, we fix a value of 0.002 in our experiments.

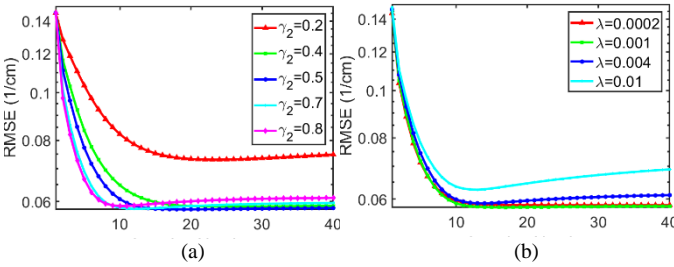


Fig. 5. RMSE curves for the BMFMR method with respect to different  $\boldsymbol{\gamma}_2$  and  $\lambda$ , respectively.

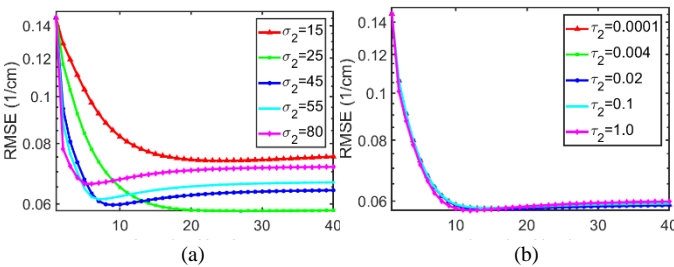


Fig. 6. RMSE curves for the BMFMR method with respect to different  $\boldsymbol{\tau}_2$  and  $\sigma_2$  respectively.

**Hard-threshold  $\boldsymbol{\tau}_2$ :** The value of  $\boldsymbol{\tau}_2$  is employed to suppress noise by removing small coefficients in the 3D transform domain. On one hand, a great value of  $\boldsymbol{\tau}_2$  will increase the anti-noising capability and smear the details in the reconstructed images. On the other hand, a small value of  $\boldsymbol{\tau}_2$  will decrease the anti-noising capability and keep more details. Therefore, the optimal value of  $\boldsymbol{\tau}_2$  should match the noise level. Fig. 6(a) shows the RMSE curves with respect to different  $\boldsymbol{\tau}_2$ . For this case, the optimal  $\boldsymbol{\tau}_2$  is around 0.01.

**Estimated noise level  $\sigma_2$ :** In this study, we investigate the effects of different estimated noise level on the image quality. Fig. 6(b) are the RMSE curves of water with respect to the iteration number for different  $\sigma_2$  values. Note that we only analyze one parameter one time and fix other parameters. From Fig. 6(b), one can see that better results can be obtained when  $\sigma_2$  is around 25. Here,  $\sigma_2$  is set as 35.

### A.3). Convergence analysis

To investigate the convergences of the proposed algorithms, the convergence curves in terms of RMSEs of water vs. iteration number are given in Fig. 7. One can see that all the optimized BMFMR can converge to a stable solution with a given RMSE. In fact, for the BMFMR material reconstruction methods, the RMSE decreases rapidly at first, and then it is subsequently stable after 15 iterations. More rigid theoretical analysis is provided in Appendix A.2.

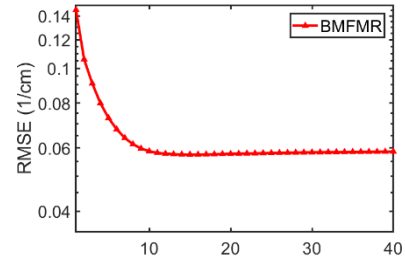


Fig. 7 RMSEs curves of water vs. iteration number.

### A.4). Computational cost

As far as the computational cost is concerned, the proposed algorithms mainly divide into three subroutines: the multi-energy projection dataset decomposition, back-projection reconstruction and regularization. The whole computational cost depends on the number of materials. The higher the number of the materials is, the larger the time consumption is. Regarding the regularization term BMF, the computational cost depends on a series of parameter settings such as the patch size, search neighborhood size, the patch sliding step, etc. In this study, all the algorithms are programmed by Matlab (version 2017b) on a PC (i7-6700, 32.0 GB memory). Here, the multi-energy projection dataset decomposition and backprojection reconstruction steps consume 77.56 and 23.90 seconds, respectively. For the TV, NLM and BMF regularization terms, they cost 0.95, 379.27 and 13.5 seconds, respectively. Obviously, the NLM regularization term requires more time than the TV and BMF regularizations.

## B. Physical Phantom Experiments

A physical phantom containing three basis materials (i.e., water, iodine and aluminum) is scanned by an experimental spectral CT system in Capital Normal University (CNU). As shown in Fig. 8, the spectral CT system includes a micro-focus x-ray source (YXLON, 225Kv) and a flat-panel PCD (Xcounter, XC-Hydra FX20). Here, the PCD consists of 2048 detector cells and each of them covers 0.1 mm. To reduce noise, every 4 cells are combined to a form a low resolution detector with 512 cells. Because the PCD only has two energy channels, the projections containing 4 different energy bins with 360 views are obtained by scanning the phantom multiple times and the voltage settings of the x-ray source is 137kV.



The distances starting from the x-ray source to object center and the PCD are 182.68 mm and 440.50 mm, respectively. Thus, the radius of FOV is 41.3 mm. In this study, the size of each reconstructed material image is  $512 \times 512$  and each pixel covers an area of  $0.162 \times 0.162 \text{ mm}^2$ .



Fig. 8. Setups of physical phantom experiments. (a) is the spectral CT system and (b) is the phantom containing five cylinders and each of them represents different basis material or different concentrations of iodine solution.

The x-ray energy spectrum plays an important role in our proposed methods and the error between the estimated and ground truth may compromise the material reconstruction results. In this study, the spectrum is estimated by manually adjusting the threshold with a small step and appropriate post-processing techniques (see Fig. 9). From Fig. 9, the x-ray spectrum starting from 13KeV to 137KeV is divided into 4 energy channels, i.e., [13, 25], (25, 33], (33, 48], (48, 137]. Note that the accuracy of spectrum distribution can directly affect the accuracy of the final reconstructed results. Again, the closer the estimated spectrum to the truth is, the higher the accuracy of reconstructed materials is. Fig. 10 shows the reconstructed three basis materials. From Fig. 10, it can be seen that some of the aluminum is wrongly classified as water. Compared with the results of MSART, TVMR and NLMMR, the BMFMR may obtain the best visual evaluation. To validate this conclusion, the ROIs 1 and 2 are further extracted to compute the index of RMSE. Here, note that the ground truth of ROIs 1 and 2 are 1 and 0 in theoretic. The quantitative evaluation results are listed in table 3. From table 3, the BMFMR can always obtain the smallest RMSE value. The RMSE values for ROI 2 are large. This is because the energy spectrum used in this study is not accurate and then it compromises the final material reconstruction results. On the other hand, there is x-ray beam hardening in this case. Similarly, due to the inaccuracy of energy spectrum, 1.5% and 1.0% iodine concentrations can be observed in all methods, but 0.5% iodine concentration is difficult to see in all reconstructed results.

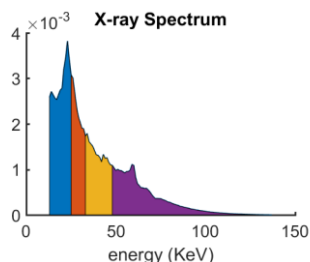


Fig.9 Estimated spectrum of a micro-focus x-ray source with the voltage setting 137kV.

Table 3. RMSE evaluation results of ROIs 1 and 2.

Material	MSART	TVMR	NLMMR	BMFMR
ROI 1	0.4346	0.4316	0.3920	<b>0.3218</b>
ROI 2	0.8623	0.8565	0.8584	<b>0.8181</b>

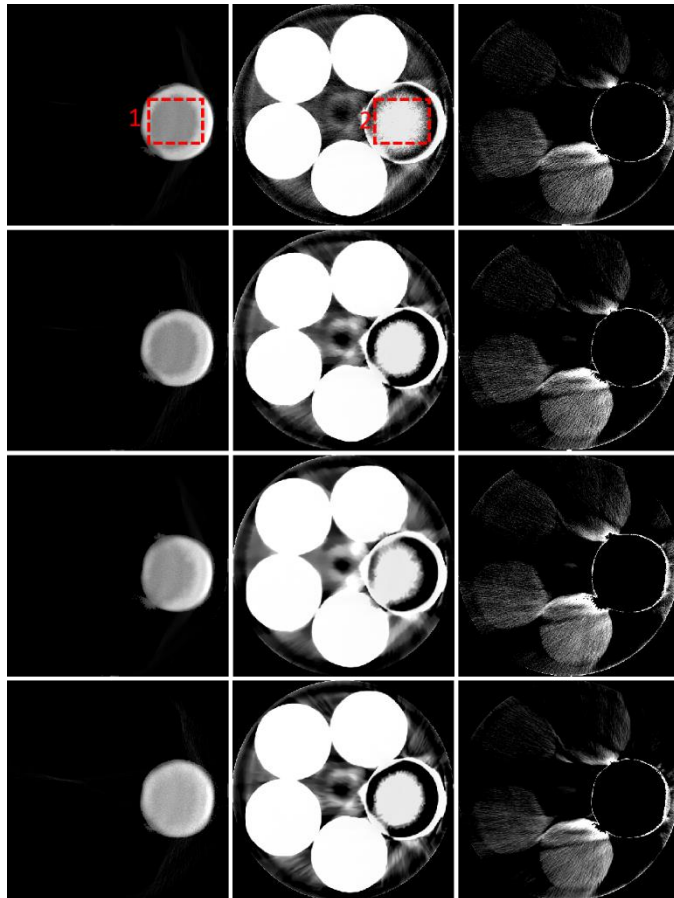


Fig. 10 Physical phantom experiment results. The 1<sup>st</sup> to 3<sup>rd</sup> column images are the reconstructed maps of aluminum, water and iodine, where the display windows are [0 1], [0 1] and [0.0001 0.015]. The 1<sup>st</sup> to 4<sup>th</sup> rows are reconstructed by the MSART, TVMR, NLMMR and BMFMR methods, respectively.

## V. CONCLUSIONS AND DISCUSSIONS

To reconstruct basis material images directly from the spectral CT projection datasets, we first propose an MSART algorithm. Compared with the E-ART method for DECT [27], the innovations of MSART are demonstrated in the following three ways. First, the MSART method is proposed by considering the spectral CT imaging model and Taylor's first-order expansion rather than the basic idea of ART. Second, the E-ART ignores the implicate relationship between projection decomposition and image reconstruction. The MSART method elaborates this relationship by introducing image constraint  $\mathbf{P} = (\mathbf{A}\mathcal{F})^T$  in Eq. (14). Third, the MSART model is strictly deduced by minimizing a higher-order Taylor expansion rather than by a simple analysis for E-ART, which can refer to Eqs. (8)-(12) and *Theorem 1* in the Appendix A.1. Next, we incorporate the TV, NLM and BMF regularizations into the MSART model to generate the TVMR, NLMMR and BMFMR algorithms. This can help to improve the robustness of the MSART method and preserve the material image edge information. Both numerical simulation and physical phantom

experiment results demonstrate that the reconstructed material images by the BMFMR method have less noise and higher accuracy compared with those reconstructed by the MSART, TVMR and NLMMR methods.

Since the accuracy of the energy spectrum can compromise the accuracy of the final material reconstructions, estimation of the energy spectrum is the largest limitation of the proposed methods in practical applications. To further analyze the effects of the energy spectrum on the final results, a numerical phantom, which is similar to the physical phantom shown in Fig. (8b), is employed. Fig. 11 shows the MSART reconstruction results in the cases of accurate and inaccurate energy spectra. From Fig. 11, it can be seen that the MSART can exactly reconstruct three basis materials with accurate spectrum distribution. While for the inaccurate spectrum, most pixels of the aluminum are wrongly classified as water and the pixels of iodine are also difficult to observe. How to improve the accuracy of the estimated spectrum is a key in our follow-up work.

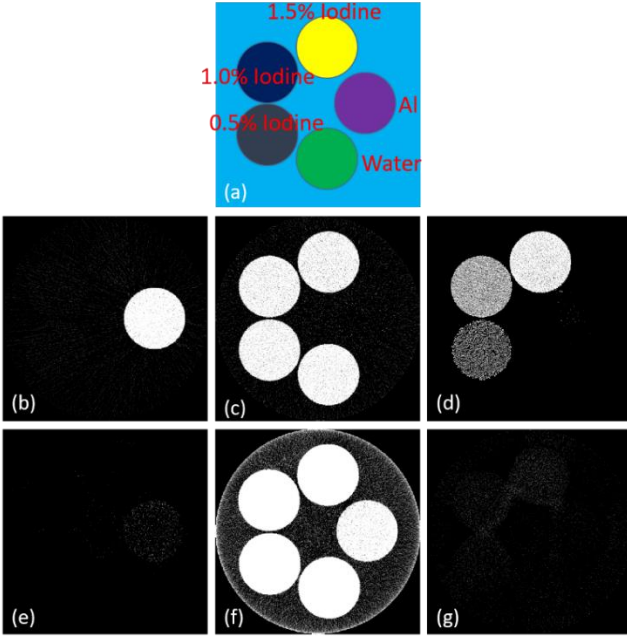


Fig. 11 Material reconstruction results from accurate and inaccurate energy spectra. (a) is the numerical phantom, (b)-(d) represent the reconstructed aluminum, water and iodine maps using MSART with accurate energy spectrum. (e)-(g) are the results with inaccurate spectrum.

Because the material reconstruction methods consider each x-ray path independently, they can suppress beam-hardening artifacts in the reconstructed material images [5]. However, the noise levels will be magnified by decomposing the average projection dataset into independent basis material contributions. Although exciting results have been achieved by incorporating the TV, NLM and BMF regularizations into the MSART model, there is still some room for improvement. For example, the quality of the reconstructed material images by the BMFMR method is still poor in the case of  $10^5$  photons per x-ray path although it is much better than that obtained by the TVMR and NLMMR methods. To further improve the accuracy of material reconstruction, in the future we will consider more constraints to optimize the solution. In our study, the parameters are selected empirically based on extensive experiments. A comprehensive evaluation to further

optimize the parameters in the BMFMR method (e.g. regularization and BMF hard-thresholding parameters) is listed in our follow-up work. We will also try some automatic schemes for parameter optimization.

In conclusion, based on Taylor's first order expansion theory, we first propose an original one-step material reconstruction algorithm MSART for spectral CT. An optimized BMFMR method is further developed to well preserve image edges and improve the robustness of MSART. This will be extremely useful for basis material reconstruction for spectral CT application.

#### ACKNOWLEDGEMENT

The authors are grateful to Mr. Joshua Lojzim at UMass Lowell for his help on language editing.

## Appendix

### A.1. Minimization of $Y(\mathbf{P})$ defined by Eq. (17)

For the objective function  $Y(\mathbf{P})$  defined by Eq. (17), we have the following Theorem.

**Theorem 1:** Let  $\lambda > 0$ ,  $Y(\mathbf{P})$  is a strictly convex function with respect to  $\mathbf{P}$  in a feasible set  $\mathbf{P} \in \mathcal{P}$ . Then,  $Y(\mathbf{P})$  can reach its global minimizer by the following iterative formula

$$\begin{aligned} & (\mathbf{P}_{\#1}^{(k+1)}, \dots, \mathbf{P}_{\#L}^{(k+1)}) = \\ & \left( \mathbf{P}_{\#1}^{(k)} - \beta_1 \left( \boldsymbol{\Theta}_{\#1\#}^{(k)T} \boldsymbol{\Theta}_{\#1\#}^{(k)} + \lambda \mathbf{J} \right)^{-1} \mathbf{S}_1^{(k)} (\bar{\mathbf{Q}}_{\#1} - \mathbf{Q}_{\#1}^{(k)}), \dots, \right. \\ & \left. \mathbf{P}_{\#L}^{(k)} - \beta_1 \left( \boldsymbol{\Theta}_{\#L\#}^{(k)T} \boldsymbol{\Theta}_{\#L\#}^{(k)} + \lambda \mathbf{J} \right)^{-1} \mathbf{S}_L^{(k)} (\bar{\mathbf{Q}}_{\#L} - \mathbf{Q}_{\#L}^{(k)}) \right), \end{aligned}$$

where  $\beta_1$  is a constant to control the step size and  $k$  indicates the iteration number.

**Proof:**  $Y(\mathbf{P})$  can be rewritten as

$$Y(\mathbf{P}) = \sum_{\ell=1}^L \left\{ \left\| \boldsymbol{\Theta}_{\#\ell\#}^{(k)} (\mathbf{P}_{\#\ell} - \mathbf{P}_{\#\ell}^{(k)}) + \mathbf{S}_{\ell}^{(k)} (\bar{\mathbf{Q}}_{\#\ell} - \mathbf{Q}_{\#\ell}^{(k)}) \right\|_F^2 + \lambda \left\| ((\mathbf{A}_{\ell\#\mathcal{F}})^T)^{(k)} - \mathbf{P}_{\#\ell} \right\|_F^2 \right\}. \quad (\text{A.1})$$

Because the measured data from each x-ray path  $\ell$  are independent, to obtain the optimized solution for Eq. (A.1), we can estimate an arbitrary  $\ell^{\text{th}}$  ( $1 \leq \ell \leq L$ ) x-ray  $\mathbf{P}_{\#\ell}$  independently. Without loss of generality, let us compute

$$\begin{aligned} \frac{\partial Y(\mathbf{P})}{\partial \mathbf{P}_{\#\ell}} &= \boldsymbol{\Theta}_{\#\ell\#}^{(k)T} \left( \boldsymbol{\Theta}_{\#\ell\#}^{(k)} (\mathbf{P}_{\#\ell} - \mathbf{P}_{\#\ell}^{(k)}) + \mathbf{S}_{\ell}^{(k)} (\bar{\mathbf{Q}}_{\#\ell} - \mathbf{Q}_{\#\ell}^{(k)}) \right) \\ &+ \lambda \left( \mathbf{P}_{\#\ell} - ((\mathbf{A}_{\ell\#\mathcal{F}})^T)^{(k)} \right). \quad (\text{A.2}) \end{aligned}$$

Let  $\partial Y(\mathbf{P}) / \partial \mathbf{P}_{\#\ell} = 0$ , ( $1 \leq \ell \leq L$ ), and we have

$$\begin{aligned} \boldsymbol{\Theta}_{\#\ell\#}^{(k)T} \left( \boldsymbol{\Theta}_{\#\ell\#}^{(k)} (\mathbf{P}_{\#\ell} - \mathbf{P}_{\#\ell}^{(k)}) + \mathbf{S}_{\ell}^{(k)} (\bar{\mathbf{Q}}_{\#\ell} - \mathbf{Q}_{\#\ell}^{(k)}) \right) \\ + \lambda \left( \mathbf{P}_{\#\ell} - ((\mathbf{A}_{\ell\#\mathcal{F}})^T)^{(k)} \right) = 0. \quad (\text{A.3}) \end{aligned}$$

It can be evolved into

$$\begin{aligned} \boldsymbol{\Theta}_{\#\ell\#}^{(k)T} \boldsymbol{\Theta}_{\#\ell\#}^{(k)} \mathbf{P}_{\#\ell} + \lambda \mathbf{P}_{\#\ell} = \\ \boldsymbol{\Theta}_{\#\ell\#}^{(k)T} \boldsymbol{\Theta}_{\#\ell\#}^{(k)} \mathbf{P}_{\#\ell}^{(k)} - \mathbf{S}_{\ell}^{(k)} (\bar{\mathbf{Q}}_{\#\ell} - \mathbf{Q}_{\#\ell}^{(k)}) + \lambda ((\mathbf{A}_{\ell\#\mathcal{F}})^T)^{(k)}. \quad (\text{A.4}) \end{aligned}$$

Note that  $\mathbf{P}_{\#\ell}^{(k)} = ((\mathbf{A}_{\ell\#\mathcal{F}})^T)^{(k)}$ . Eq. (A.4) can be simplified as

$$\begin{aligned} \left( \boldsymbol{\Theta}_{\#\ell\#}^{(k)T} \boldsymbol{\Theta}_{\#\ell\#}^{(k)} + \lambda \mathbf{J} \right) \mathbf{P}_{\#\ell} \\ = \left( \boldsymbol{\Theta}_{\#\ell\#}^{(k)T} \boldsymbol{\Theta}_{\#\ell\#}^{(k)} + \lambda \mathbf{J} \right) \mathbf{P}_{\#\ell}^{(k)} - \mathbf{S}_{\ell}^{(k)} (\bar{\mathbf{Q}}_{\#\ell} - \mathbf{Q}_{\#\ell}^{(k)}), \quad (\text{A.5}) \end{aligned}$$

where  $\mathbf{J}$  represents the identity transform whose size is the same as  $\mathbf{\Theta}_{\#\ell\#}^{(k)T} \mathbf{\Theta}_{\#\ell\#}^{(k)}$ . Since  $\lambda > 0$ , the matrix  $\mathbf{\Theta}_{\#\ell\#}^{(k)T} \mathbf{\Theta}_{\#\ell\#}^{(k)} + \lambda \mathbf{J}$  is always reversible. The solution of  $\mathbf{P}_{\#\ell}$  can be iteratively updated as follow

$$\mathbf{P}_{\#\ell}^{(k+1)} = \mathbf{P}_{\#\ell}^{(k)} - \beta_1 \left( \mathbf{\Theta}_{\#\ell\#}^{(k)T} \mathbf{\Theta}_{\#\ell\#}^{(k)} + \lambda \mathbf{J} \right)^{-1} \mathbf{S}_\ell^{(k)} (\bar{\mathbf{Q}}_{\#\ell} - \mathbf{Q}_{\#\ell}^{(k)}), \quad (\text{A.6})$$

where  $\left( \mathbf{\Theta}_{\#\ell\#}^{(k)T} \mathbf{\Theta}_{\#\ell\#}^{(k)} + \lambda \mathbf{J} \right)^{-1}$  is the inverse matrix of the  $\left( \mathbf{\Theta}_{\#\ell\#}^{(k)T} \mathbf{\Theta}_{\#\ell\#}^{(k)} + \lambda \mathbf{J} \right)$  and  $\beta_1$  is a relaxation factor in (0,2). Thus, we can obtain such a current stationary point  $\mathbf{p} = (\mathbf{P}_{1\#}^{(k+1)}, \dots, \mathbf{P}_{L\#}^{(k+1)})$ , which can be given as

$$\mathbf{p} = \begin{pmatrix} \mathbf{P}_{\#1}^{(k)} - \beta_1 \left( \left( \mathbf{\Theta}_{\#1\#}^{(k)T} \mathbf{\Theta}_{\#1\#}^{(k)} + \lambda \mathbf{J} \right) \right)^{-1} \mathbf{S}_1^{(k)} (\bar{\mathbf{Q}}_{\#1} - \mathbf{Q}_{\#1}^{(k)}) \\ \vdots \\ \mathbf{P}_{\#L}^{(k)} - \beta_1 \left( \left( \mathbf{\Theta}_{\#L\#}^{(k)T} \mathbf{\Theta}_{\#L\#}^{(k)} + \lambda \mathbf{J} \right) \right)^{-1} \mathbf{S}_L^{(k)} (\bar{\mathbf{Q}}_{\#L} - \mathbf{Q}_{\#L}^{(k)}) \end{pmatrix}^T. \quad (\text{A.7})$$

However, the convergence point of such a  $\mathbf{p}$  is only a stationary point and it cannot be guaranteed as the global minimization point. To ensure the current point  $\mathbf{p}$  is the optimization minimization point, it is necessary to compute the Hessian matrix  $\mathcal{H}$  of  $Y(\mathbf{P})$

$$\mathcal{H} = \begin{bmatrix} \frac{\partial^2 Y(\mathbf{P})}{\partial \mathbf{P}_{\#1} \partial \mathbf{P}_{\#1}} & \dots & \frac{\partial^2 Y(\mathbf{P})}{\partial \mathbf{P}_{\#1} \partial \mathbf{P}_{\#L}} \\ \vdots & \ddots & \vdots \\ \frac{\partial^2 Y(\mathbf{P})}{\partial \mathbf{P}_{\#L} \partial \mathbf{P}_{\#1}} & \dots & \frac{\partial^2 Y(\mathbf{P})}{\partial \mathbf{P}_{\#L} \partial \mathbf{P}_{\#L}} \end{bmatrix}, \quad (\text{A.8})$$

where  $\mathcal{H} \in \mathcal{R}^{Z \times Z}$  and  $Z = L \times N \times N$ . Because each of x-ray is independent, that means

$$\frac{\partial^2 Y(\mathbf{P})}{\partial \mathbf{P}_{\#\ell} \partial \mathbf{P}_{\#j}} = \frac{\partial \left( \mathbf{\Theta}_{\#\ell\#}^{(k)T} \left( \mathbf{\Theta}_{\#\ell\#}^{(k)} (\mathbf{P}_{\#\ell} - \mathbf{P}_{\#\ell}^{(k)}) + (\bar{\mathbf{Q}}_{\#\ell} - \mathbf{Q}_{\#\ell}^{(k)}) \right) + \lambda (\mathbf{P}_{\#\ell} - ((\mathbf{A}_{\ell\#} \mathcal{F})^T)^{(k)}) \right)}{\partial \mathbf{P}_{\#j}} = \begin{cases} \mathbf{\Theta}_{\#\ell\#}^{(k)T} \mathbf{\Theta}_{\#\ell\#}^{(k)} + \lambda \mathbf{J}, & \ell = j, \\ \mathbf{0}, & \text{otherwise,} \end{cases} \quad (\text{A.9})$$

where  $\mathbf{0}$  stands for a zero matrix in  $\mathcal{R}^{N \times N}$ . Thus, the Hessian matrix  $\mathcal{H}$  can be further converted into

$$\begin{aligned} \mathcal{H} &= \begin{bmatrix} \mathbf{\Theta}_{\#1\#}^{(k)T} \mathbf{\Theta}_{\#1\#}^{(k)} + \lambda \mathbf{J} & \dots & \mathbf{0} \\ \vdots & \ddots & \vdots \\ \mathbf{0} & \dots & \mathbf{\Theta}_{\#L\#}^{(k)T} \mathbf{\Theta}_{\#L\#}^{(k)} + \lambda \mathbf{J} \end{bmatrix} \\ &= \begin{bmatrix} \mathbf{\Theta}_{\#1\#}^{(k)T} \mathbf{\Theta}_{\#1\#}^{(k)} & \dots & \mathbf{0} \\ \vdots & \ddots & \vdots \\ \mathbf{0} & \dots & \mathbf{\Theta}_{\#L\#}^{(k)T} \mathbf{\Theta}_{\#L\#}^{(k)} \end{bmatrix} + \lambda \mathbf{J} \\ &= \begin{bmatrix} \mathbf{\Theta}_{\#1\#}^{(k)} & \dots & \mathbf{0} \\ \vdots & \ddots & \vdots \\ \mathbf{0} & \dots & \mathbf{\Theta}_{\#L\#}^{(k)} \end{bmatrix}^T \begin{bmatrix} \mathbf{\Theta}_{\#1\#}^{(k)} & \dots & \mathbf{0} \\ \vdots & \ddots & \vdots \\ \mathbf{0} & \dots & \mathbf{\Theta}_{\#L\#}^{(k)} \end{bmatrix} + \lambda \mathbf{J} \\ &= \mathcal{H}_1^T \mathcal{H}_1 + \lambda \mathbf{J} > \mathbf{0}, \end{aligned} \quad (\text{A.10})$$

where  $\lambda > 0$ . Because the Hessian matrix  $\mathcal{H}$  of  $Y(\mathbf{P})$  is always greater than 0 and is a positive definite matrix, the global minimization point of  $Y(\mathbf{P})$  exists and it can be

iteratively determined by Eq. (A.6), which completes the proof of *Theorem 1*. ■

## A. 2. Theoretical analysis of the BMFMR algorithm

Because the objective function is monotonically minimized in all the steps of the alternating optimization process, the value of the objective function should be monotonically decreased for the proposed BMFMR algorithm. Since Eq. (18) monotonically minimizes the objective function (17), according to *Theorem 1*, we have

$$\begin{aligned} & \sum_{\ell=1}^L \left\{ \left\| \mathbf{\Theta}_{\#\ell\#}^{(k)} (\mathbf{P}_{\#\ell}^{(k+1)} - \mathbf{P}_{\#\ell}^{(k)}) + \mathbf{S}_\ell^{(k)} (\bar{\mathbf{Q}}_{\#\ell} - \mathbf{Q}_{\#\ell}^{(k)}) \right\|_F^2 \right. \\ & \quad \left. + \lambda \left\| ((\mathbf{A}_{\ell\#} \mathcal{F})^T)^{(k)} - \mathbf{P}_{\#\ell}^{(k+1)} \right\|_F^2 \right\} \\ & \leq \sum_{\ell=1}^L \left\{ \left\| \mathbf{\Theta}_{\#\ell\#}^{(k-1)} (\mathbf{P}_{\#\ell}^{(k)} - \mathbf{P}_{\#\ell}^{(k-1)}) + \mathbf{S}_\ell^{(k-1)} (\bar{\mathbf{Q}}_{\#\ell} - \mathbf{Q}_{\#\ell}^{(k-1)}) \right\|_F^2 \right. \\ & \quad \left. + \lambda \left\| ((\mathbf{A}_{\ell\#} \mathcal{F})^T)^{(k-1)} - \mathbf{P}_{\#\ell}^{(k)} \right\|_F^2 \right\}, \\ & \quad \forall k = 2, 3 \dots K. \end{aligned} \quad (\text{A.11})$$

Considering Eq. (30) monotonically minimizes the objective function (29a), according to the steepest descent theory, we can obtain

$$\begin{aligned} & \left\| \mathbf{A} \mathbf{f}_n^{(k+1)} - (\mathbf{P}_{n\#}^{(k+1)})^T \right\|_F^2 + \gamma_n \left\| \mathbf{f}_n^{(k+1)} - \mathbf{g}_n^{(k)} - \mathbf{t}_n^{(k)} \right\|_F^2 \\ & \leq \left\| \mathbf{A} \mathbf{f}_n^{(k)} - (\mathbf{P}_{n\#}^{(k+1)})^T \right\|_F^2 + \gamma_n \left\| \mathbf{f}_n^{(k)} - \mathbf{g}_n^{(k)} - \mathbf{t}_n^{(k)} \right\|_F^2, \\ & \quad \forall n = 1, \dots, N. \end{aligned} \quad (\text{A.12})$$

As for Eq. (29b), it can be divided into a data fidelity term and a regularization term. On one hand, the  $\Phi_n(\mathbf{g}_n)$  can be considered as the 3D transform coefficient  $\mathcal{W}_n$ . Thus, Eq. (29b) can be read as

$$\min_{\mathbf{g}_n} \left\| \mathbf{f}_n^{(k+1)} - \mathbf{g}_n - \mathbf{t}_n^{(k)} \right\|_F^2, \quad s.t. \mathcal{W}_n \leq L_n, \quad \forall n = 1, \dots, N, \quad (\text{A.13})$$

where  $L_n$  represents the 3D transform level. Clearly, the solution of problem (A.13) satisfies

$$\left\| \mathbf{f}_n^{(k+1)} - \mathbf{g}_n^{(k+1)} - \mathbf{t}_n^{(k)} \right\|_F^2 \leq \left\| \mathbf{f}_n^{(k+1)} - \mathbf{g}_n^{(k)} - \mathbf{t}_n^{(k)} \right\|_F^2. \quad (\text{A.14})$$

On the other hand, the hard thresholding method was employed to minimize problem (29b) in the regularization step. Thus, we have

$$\begin{aligned} & \gamma_n \left\| \mathbf{f}_n^{(k+1)} - \mathbf{g}_n^{(k+1)} - \mathbf{t}_n^{(k)} \right\|_F^2 + \tau_n \left\| \Phi_n(\mathbf{g}_n^{(k+1)}) \right\|_0 \\ & \leq \gamma_n \left\| \mathbf{f}_n^{(k+1)} - \mathbf{g}_n^{(k)} - \mathbf{t}_n^{(k)} \right\|_F^2 + \tau_n \left\| \Phi_n(\mathbf{g}_n^{(k)}) \right\|_0, \\ & \quad \forall n = 1, \dots, N. \end{aligned} \quad (\text{A.15})$$

Noting that Eq. (31) monotonically reduces the value of (29c), we have

$$\left\| \mathbf{f}_n^{(k+1)} - \mathbf{g}_n^{(k+1)} - \mathbf{t}_n^{(k+1)} \right\|_F^2 \leq \left\| \mathbf{f}_n^{(k+1)} - \mathbf{g}_n^{(k+1)} - \mathbf{t}_n^{(k)} \right\|_F^2, \quad \forall n = 1, \dots, N. \quad (\text{A.16})$$

From formulae (A.12)-(A.16), we can obtain

$$\begin{aligned} & \left\| \mathbf{A} \mathbf{f}_n^{(k+1)} - (\mathbf{P}_{n\#}^{(k+1)})^T \right\|_F^2 + \gamma_n \left\| \mathbf{f}_n^{(k+1)} - \mathbf{g}_n^{(k+1)} - \mathbf{t}_n^{(k+1)} \right\|_F^2 \\ & \quad + \tau_n \left\| \Phi_n(\mathbf{g}_n^{(k+1)}) \right\|_0 \\ & \leq \left\| \mathbf{A} \mathbf{f}_n^{(k)} - (\mathbf{P}_{n\#}^{(k+1)})^T \right\|_F^2 + \gamma_n \left\| \mathbf{f}_n^{(k)} - \mathbf{g}_n^{(k)} - \mathbf{t}_n^{(k)} \right\|_F^2 \\ & \quad + \tau_n \left\| \Phi_n(\mathbf{g}_n^{(k)}) \right\|_0. \end{aligned} \quad (\text{A.17})$$

Combining Eqs. (A.11) and (A.17), finally it shows that the BMFMR monotonically reduces its objective function. It is

necessary to emphasize that the aforementioned monotonic reduction of the objective function cannot guarantee the convergence of the reconstruction algorithms and the BMFMR. Because the reconstruction model of Eq. (24) contains the  $L_0$ -norm minimization of 3D transform coefficients, the proof of the convergence of BMFMR algorithm is difficult, and thus out of the scope of this study.

## REFERENCES

- [1] K. Kim *et al.*, "Sparse-view spectral CT reconstruction using spectral patch-based low-rank penalty," *IEEE transactions on medical imaging*, vol. 34, no. 3, pp. 748-760, 2015.
- [2] T. R. Johnson *et al.*, "Material differentiation by dual energy CT: initial experience," *European radiology*, vol. 17, no. 6, pp. 1510-1517, 2007.
- [3] H. Saito *et al.*, "Reduced iodinated contrast media for abdominal imaging by dual-layer spectral detector computed tomography for patients with kidney disease," *Radiology Case Reports*, vol. 13, no. 2, pp. 437-443, 2018/04/01/ 2018.
- [4] Y. Liu *et al.*, "Feasibility of spectral imaging with low - concentration contrast medium in abdominal CT angiography of obese patients," *International journal of clinical practice*, vol. 70, no. 9B, 2016.
- [5] R. F. Barber, E. Y. Sidky, T. G. Schmidt, and X. Pan, "An algorithm for constrained one-step inversion of spectral CT data," *Physics in Medicine & Biology*, vol. 61, no. 10, p. 3784, 2016.
- [6] R. E. Alvarez and A. Macovski, "Energy-selective reconstructions in x-ray computerised tomography," *Physics in Medicine & Biology*, vol. 21, no. 5, p. 733, 1976.
- [7] H. Huang, F. Luo, J. Liu, and Y. Yang, "Dimensionality reduction of hyperspectral images based on sparse discriminant manifold embedding," *ISPRS Journal of Photogrammetry and Remote Sensing*, vol. 106, pp. 42-54, 2015.
- [8] F. Luo, H. Huang, Z. Ma, and J. Liu, "Semisupervised sparse manifold discriminative analysis for feature extraction of hyperspectral images," *IEEE Transactions on Geoscience and Remote Sensing*, vol. 54, no. 10, pp. 6197-6211, 2016.
- [9] P. He, B. Wei, W. Cong, and G. Wang, "Optimization of K - edge imaging with spectral CT," *Medical physics*, vol. 39, no. 11, pp. 6572-6579, 2012.
- [10] G. N. Hounsfield, "Computerized transverse axial scanning (tomography): Part 1. Description of system," *The British journal of radiology*, vol. 46, no. 552, pp. 1016-1022, 1973.
- [11] Y. Zhang, X. Mou, G. Wang, and H. Yu, "Tensor-based dictionary learning for spectral CT reconstruction," *IEEE transactions on medical imaging*, vol. 36, no. 1, pp. 142-154, 2017.
- [12] Q. Wang, Y. Zhu, and H. Yu, "Locally linear constraint based optimization model for material decomposition," *Physics in Medicine & Biology*, vol. 62, no. 21, p. 8314, 2017.
- [13] W. Wu, Y. Zhang, Q. Wang, F. Liu, P. Chen, and H. Yu, "Low-dose spectral CT reconstruction using image gradient  $l_0$ -norm and tensor dictionary," *Applied Mathematical Modelling*, vol. 63, pp. 538-557, 2018/11/01/ 2018.
- [14] W. Wu, H. Yu, S. Wang, and F. Liu, "BPF-type region-of-interest reconstruction for parallel translational computed tomography," *Journal of X-ray science and technology*, vol. 25, no. 3, pp. 487-504, 2017.
- [15] W. Wu, H. Yu, W. Cong, and F. Liu, "Theoretically exact backprojection filtration algorithm for multi-segment linear trajectory," *Physics in Medicine & Biology*, vol. 63, no. 1, p. 015037, 2018.
- [16] K. Taguchi and J. S. Iwaczyk, "Vision 20/20: Single photon counting x - ray detectors in medical imaging," *Medical physics*, vol. 40, no. 10, 2013.
- [17] Q. Xu *et al.*, "Image reconstruction for hybrid true-color micro-CT," *IEEE transactions on biomedical engineering*, vol. 59, no. 6, pp. 1711-1719, 2012.
- [18] B. Zhao, H. Gao, H. Ding, and S. Molloi, "Tight - frame based iterative image reconstruction for spectral breast CT," *Medical physics*, vol. 40, no. 3, 2013.
- [19] S. Leng, L. Yu, J. Wang, J. G. Fletcher, C. A. Mistretta, and C. H. McCollough, "Noise reduction in spectral CT: Reducing dose and breaking the trade - off between image noise and energy bin selection," *Medical physics*, vol. 38, no. 9, pp. 4946-4957, 2011.
- [20] Z. Yu, S. Leng, Z. Li, and C. H. McCollough, "Spectral prior image constrained compressed sensing (spectral PICCS) for photon-counting computed tomography," *Physics in Medicine & Biology*, vol. 61, no. 18, p. 6707, 2016.
- [21] H. Gao, H. Yu, S. Osher, and G. Wang, "Multi-energy CT based on a prior rank, intensity and sparsity model (PRISM)," *Inverse problems*, vol. 27, no. 11, p. 115012, 2011.
- [22] S. Niu, G. Yu, J. Ma, and J. Wang, "Nonlocal low-rank and sparse matrix decomposition for spectral CT reconstruction," *Inverse Problems*, vol. 34, no. 2, p. 024003, 2018.
- [23] W. Wu, Y. Zhang, Q. Wang, F. Liu, F. Luo, and H. Yu, "Spatial-Spectral Cube Matching Frame for Spectral CT Reconstruction," *inverse problems*, vol. 34, no. 10, p. 104003, 2018.
- [24] W. Wu, F. Liu, Y. Zhang, Q. Wang, and H. Yu, "Non-local Low-rank Cube-based Tensor Factorization for Spectral CT Reconstruction," *arXiv preprint arXiv:1807.10610*, 2018.
- [25] R. A. Brooks, "A quantitative theory of the Hounsfield unit and its application to dual energy scanning," *Journal of computer assisted tomography*, vol. 1, no. 4, pp. 487-493, 1977.
- [26] J. Liu, H. Ding, S. Molloi, X. Zhang, and H. Gao, "TICMR: Total image constrained material reconstruction via nonlocal total variation regularization for spectral CT," *IEEE transactions on medical imaging*, vol. 35, no. 12, pp. 2578-2586, 2016.
- [27] Y. Zhao, X. Zhao, and P. Zhang, "An extended algebraic reconstruction technique (E-ART) for dual spectral CT," *IEEE Trans Med Imaging*, vol. 34, no. 3, pp. 761-8, Mar 2015.
- [28] Y. Long and J. A. Fessler, "Multi-material decomposition using statistical image reconstruction for spectral CT," *IEEE transactions on medical imaging*, vol. 33, no. 8, pp. 1614-1626, 2014.
- [29] K. Dabov, A. Foi, V. Katkovnik, and K. O. Egiazarian, "Image restoration by sparse 3D transform-domain collaborative filtering," in *Image Processing: Algorithms and Systems*, 2008, p. 681207.
- [30] K. Dabov, A. Foi, V. Katkovnik, and K. Egiazarian, "Image Denoising by Sparse 3-D Transform-Domain Collaborative Filtering," *IEEE Transactions on Image Processing*, vol. 16, no. 8, pp. 2080-2095, 2007.
- [31] A. Danielyan, V. Katkovnik, and K. Egiazarian, "BM3D frames and variational image deblurring," *IEEE Trans Image Process*, vol. 21, no. 4, pp. 1715-28, Apr 2012.
- [32] M. Salehjahromi, Y. Zhang, and H. Yu, "A spectral CT denoising algorithm based on weighted block matching 3D filtering," in *Developments in X-Ray Tomography XI*, 2017, vol. 10391, p. 103910G: International Society for Optics and Photonics.
- [33] E. M. Eksioğlu, "Decoupled algorithm for mri reconstruction using nonlocal block matching model: Bm3d-mri," *Journal of Mathematical Imaging and Vision*, vol. 56, no. 3, pp. 430-440, 2016.
- [34] J. H. Hubbell and S. M. Seltzer, "Tables of X-ray mass attenuation coefficients and mass energy-absorption coefficients 1 keV to 20 MeV for elements Z= 1 to 92 and 48 additional substances of dosimetric interest," National Inst. of Standards and Technology-PL, Gaithersburg, MD (United States). Ionizing Radiation Div.1995.
- [35] S. Setzer, "Operator splittings, Bregman methods and frame shrinkage in image processing," *International Journal of Computer Vision*, vol. 92, no. 3, pp. 265-280, 2011.
- [36] W. Wu, H. Yu, C. Gong, and F. Liu, "Swinging multi-source industrial CT systems for aperiodic dynamic imaging," *Optics express*, vol. 25, no. 20, pp. 24215-24235, 2017.